

Supporting information

Oriented Attachment and Activated Dipoles leading to Anisotropic H-Bond-Free Self-Assembly of n-Acene Derivatives into Organic Nanoribbons Emitting Linearly Polarized Blue Light

Philip Schäfer,¹ Leire Gartzia-Rivero,^{1,2} Min-Tzu Kao,¹ Christian Schäfer,¹ Stéphane Massip,³
Christiaan de Vet,¹ Guillaume Raffy,¹ André Del Guerso^{1,*}

1 Univ Bordeaux, CNRS, Bordeaux INP, Institut des Sciences Moléculaires, UMR5255, 33400 Talence, France

2 Department of Physical Chemistry, University of the Basque Country (UPV/EHU), Apartado 644, 48080 Bilbao, Spain

3 IECB, Univ Bordeaux, CNRS UMS3033, INSERM US001, F-33607 Pessac, France

Chemicals and Synthesis

Commercially available chemicals, such as solvents, were used without further purification. Tetrahydrofuran was distilled over sodium prior to use. Petroleum ether (PET) with a boiling range of 40-60°C was used.

The precursors 2,3-dihydroxy-anthraquinone and 2,3-dialkyloxy-anthraquinones were synthesized according to known procedures.¹ The general procedure for the synthesis of 2,3-dialkyloxy-9,10-diphenyl-anthracenes was the following. 0.5 mmol 2,3-dialkyloxy-anthraquinone were dissolved/suspended in 25 mL THF under argon and cooled down in an ice bath. PhLi (1.8 M in cyclohexane/Et₂O 7:3, 5 equiv.) was added dropwise and the solution stirred in the melting ice bath for 18 h. Afterwards, the reaction was poured in a solution of NH₄Cl and extracted with Et₂O several times. The combined organic layers were washed with water and brine, dried over MgSO₄ and the solvent was removed *in vacuo*. The residue was dissolved in Et₂O, heated to reflux and HI (57% in H₂O, 1 mL per 0.15 mmol quinone) was added dropwise. The reaction was stirred at reflux for another 15 min, then was allowed to cool down and poured into a solution of Na₂S₂O₅. The product was extracted with DCM. The organic layer was washed with water and brine, dried over MgSO₄ and the solvent was removed *in vacuo*. The product was isolated by column chromatography on silica gel and crystallized from DCM/MeOH to obtain it as a colorless solid if necessary.

2,3-dihexadecyloxy-9,10-diphenyl-anthracene (DPA16):

Eluent: DCM/PET 1:5 (flash chromatography). Yield: 50%.

¹H-NMR (CDCl₃, 300 MHz): δ(ppm) = 0.87 (t, ³J=6.7 Hz, 6 H, CH₃), 1.20-1.45 (m, 52 H, CH₂), 1.74 (m, 4 H, CH₂), 3.84 (t, ³J=6.6 Hz, 4 H, OCH₂), 6.84 (s, 2 H, ArH), 7.24 (m, 2 H, ArH), 7.44-7.64 (m, 12 H, ArH).

¹³C-NMR (CDCl₃, 300 MHz): δ(ppm) = 14.12 (CH₃), 22.69 (CH₂), 25.99 (CH₂), 28.72 (CH₂), 29.37 (CH₂), 29.41 (CH₂), 29.62 (CH₂), 29.67 (CH₂), 29.72 (CH₂), 31.92 (CH₂), 68.39 (OCH₂), 105.16 (C_{Ar}H), 124.01 (C_{Ar}H), 126.43 (C_{Ar}H), 126.93 (C_{Ar,q}), 127.29 (C_{Ar}H), 128.47 (C_{Ar}H), 128.97 (C_{Ar,q}), 131.21 (C_{Ar}H), 134.62 (C_{Ar,q}), 139.59 (C_{Ar,q}), 149.34 (C_{Ar,q}).

HRMS (ESI, positive ions): calc. for [C₅₈H₈₂O₂+Na]⁺: 833.6207; measured: 833.6166.

2,3-dioctyloxy-9,10-diphenyl-anthracene (DPA8):

Eluent: DCM/PET 1:4. Yield: 62%.

¹H-NMR (CDCl₃, 300 MHz): δ(ppm) = 0.93 (t, ³J=6.7 Hz, 6 H, CH₃), 1.25-1.50 (m, 20 H, CH₂), 1.81 (m, 4 H, CH₂), 3.90 (t, ³J=6.6 Hz, 4 H, OCH₂), 6.91 (s, 2 H, ArH), 7.28 (m, 2 H, ArH), 7.49-7.69 (m, 12 H, ArH).

¹³C-NMR (CDCl₃, 300 MHz): δ(ppm) = 14.08 (CH₃), 22.64 (CH₂), 25.99 (CH₂), 28.73 (CH₂), 29.25 (CH₂), 29.33 (CH₂), 31.78 (CH₂), 68.37 (OCH₂), 105.19 (C_{Ar}H), 124.01 (C_{Ar}H), 126.41 (C_{Ar}H), 126.93 (C_{Ar,q}), 127.28 (C_{Ar}H), 128.46 (C_{Ar}H), 128.97 (C_{Ar,q}), 131.19 (C_{Ar}H), 134.62 (C_{Ar,q}), 139.60 (C_{Ar,q}), 149.36 (C_{Ar,q}).

HRMS (ESI, positive ions): calc. for [C₄₂H₅₀O₂+Na]⁺: 609.3703; measured: 609.3733.

Spectroscopy of DPA8 and DPA16 in solution

Table S1: Characteristic absorption wavelengths, emission wavelengths, fluorescence quantum yields, lifetimes, radiative and non-radiative constants of DPA8 and DPA16 in THF at room temperature.

Molecule	Absorption			Fluorescence			
	$\lambda_{\max, 0-0}^{\text{abs}}$ /nm	$\epsilon_{\lambda_{\max}}$ / $\times 10^4 \text{ M}^{-1} \text{ cm}^{-1}$	$\lambda_{0-0, \max}^{\text{em}}$ /nm	Φ_{em} ^{a,b}	τ /ns	k_{r} / $\times 10^8 \text{ s}^{-1}$	k_{nr} / $\times 10^7 \text{ s}^{-1}$
DPA8	373, 394	1.14	413, 433	0.76	6.9	1.1	3.5
DPA16	373, 394	1.00	413, 433	0.75	6.9	1.1	3.6

^a Samples in deoxygenated THF ($1.0 \times 10^{-5} \text{ M}$), excitation at 373 nm.

^b Measured with 9,10-diphenyl-anthracene in deoxygenated cyclohexane as reference

Crystallography

The crystal structure of DPA8 was registered in the Cambridge Crystallographic Data Centre (CCDC) database under the reference CCDC (2013401).

DPA8 crystals were obtained by the vapor deposition technique, in which the compound is dissolved in DCM in a small vial, which is inserted in a bigger vial filled with methanol. The methanol vapors will slowly mix with DCM and result in slow crystal growth.

Crystallographic data of DAP8 were collected at 293 K with a R-Axis Rapid Rigaku MSC diffractometer with monochromatic Cu-K α radiation ($\lambda = 1.54178 \text{ \AA}$) and a curved image plate detector. The unit cell determination and data reduction were performed using the Crystal Clear program suite² on

the full set of data. The structure was solved by direct methods and refined using Shelx suite of programs³ in the integrated WinGX system.⁴ The positions of the H atoms were deduced from coordinates of the non-H atoms and confirmed by Fourier synthesis. The non-H atoms were refined with anisotropic temperature parameters. H atoms were included for structure factor calculations but not refined.⁵ The program Mercury was used for analysis and drawing figures.

Table S2: Crystal structure of DPA8. Crystal system (Cs) : m = monoclinic; Vu :Volume per unit cell; Mu: Molecules per unit cell; Vm: Volume per molecule; d: calculated density; Angle(s) between anthracene layers α

	Cs	Space group	Vu Å ³	Mu	Vm Å ³	d g/cm ³	α °	Unit cell characteristics		
								a, b, c in Å	α, β, γ in °	
DPA8	m	P2 ₁ /a	3524.1	4	881	1.106	166	a = 9.4170	b = 20.5010	c = 18.2540
								$\alpha = 90$	$\beta = 90.015$	$\gamma = 90$

Green emissive doped DPA16 ribbons:

A more detailed study will be presented elsewhere. To prepare the undoped and doped AF ribbons, 100 μ l of a stock solution containing DPA16 (5.0 mM) and 6,11-diphenyl-2,3-dihexadecyltetracene (0.005 to 0.10 mM) in the good solvent DCM was quickly injected into the poor solvent MeOH (5.0 mL). The resulting solution was allowed to ripen overnight on standing in the dark and yielded a suspension of nanoribbons (see photo in Figure 2). The photo in Figure 2 was taken with 2.0% tetracene doping. The polarization data were obtained with 0.5% tetracene doping, in which case the blue emission of DPA16 is partially quenched (by 64% relative to undoped ribbons) and the emission intensity at 502 nm (I_{502}) of the tetracene is higher by a ratio $I_{502}/I_{431} = 3.2$ as compared to the emission of DPA16 at 431 nm (I_{431}). P values for the blue spectral region are obtained with a bandpass filter 425 ± 25 nm and in the green spectral region with a long-pass filter >500 nm.

Quantum mechanical calculations

Potential energy surface (PES) analyses of the DPA8 were performed with density functional theory (DFT), rotating both dihedral angles at the oxygens in 9 steps of 20° with the corresponding geometry optimization at each point (relaxed PES scan). The hybrid density functional method B3LYP was employed in conjunction with the double basis set (6-31G) using the Gaussian 09 software. All the calculations were carried out considering the solvent effect (methanol) by means of the Polarizable Continuum Model (PCM) using the integral equation formalism variant (IEFPCM), default of the SCRF (self-consistent reaction file) method. The charge density was simulated by the CHelpG method, which fits the charge of each atom to the molecular electrostatic potential.

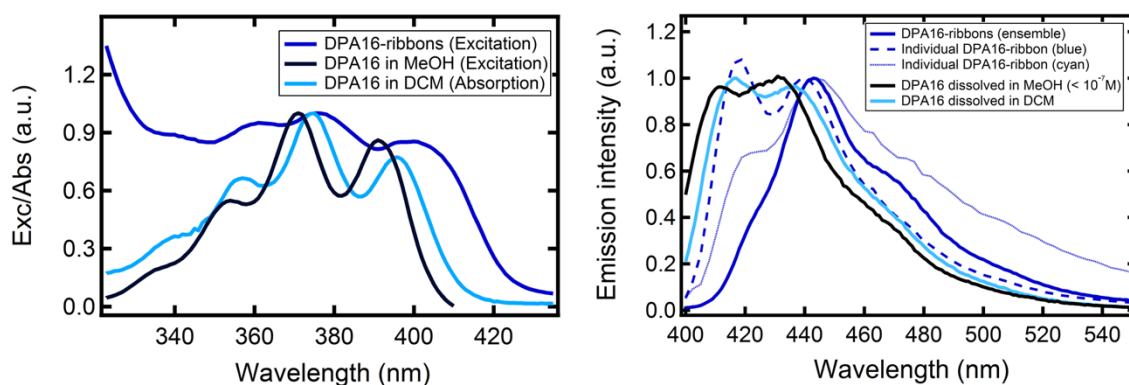


Figure S1. (left) Excitation and absorption spectra of DPA16 dissolved in DCM (cyan) and dilute in MeOH ($< 10^{-7}$ M, black), as well as of DPA16 AF ribbons self-assembled in MeOH:DCM (1.0×10^{-4} M, blue). (right) Emission spectra of DPA16 dissolved in DCM and MeOH compared with emission of DPA16 AF ribbons in the ensemble and individual ribbons, one blue emissive (dashed curve) and another more cyan-blue emissive (solid curve).

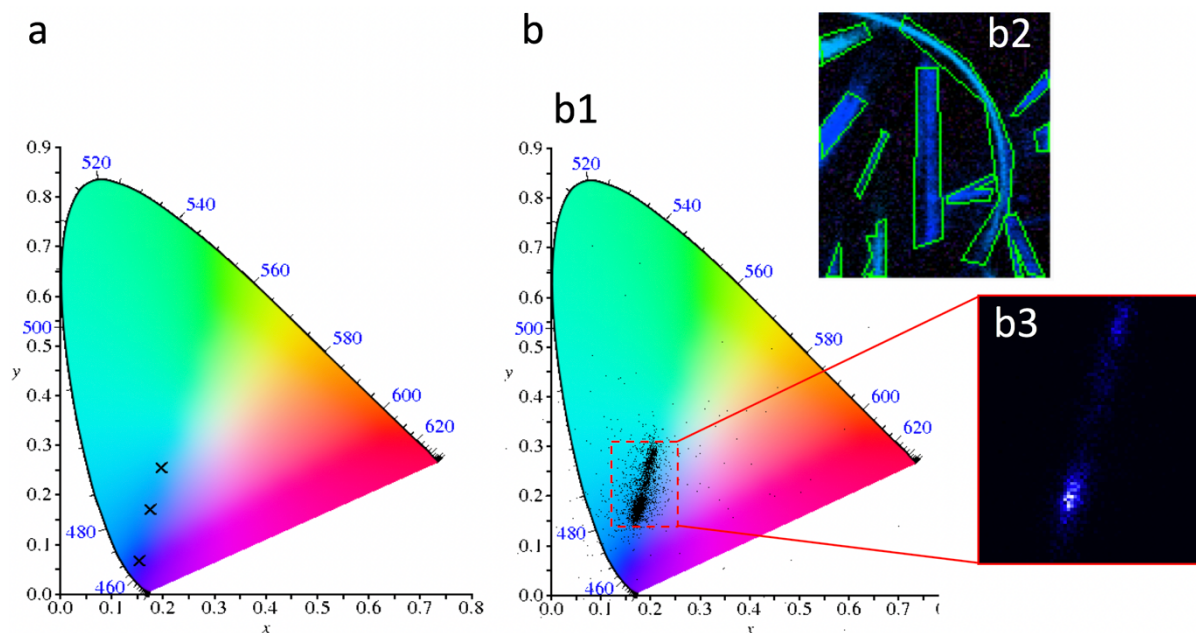


Figure S2. (a) CIE coordinates of an AR ribbon (from Fig. 1a): $x=0.1579$, $y=0.0655$; CIE coordinates of two AF ribbons (from Fig. 1b): $x=0.1798$, $y=0.1697$; $x=0.2023$, $y=0.2540$. (b) **b1** CIE coordinates of each pixel of AF ribbons (areas included in green lines **b2**, from Fig. 1b); **b3** Emission intensity for each CIE coordinate represented in graph **b1** (color scale goes from black to blue to white). Coordinates and intensity for blue and cyan AF ribbons: blue: $x = 0.180 \pm 0.004$; $y = 0.172 \pm 0.008$ (2.192×10^6 photon counts); cyan: $x = 0.208 \pm 0.004$; $y = 0.276 \pm 0.010$ (1.302×10^6 photon counts). Intensity weighted average CIE coordinates for this Image **b2**: $x = 0.190$; $y = 0.211$.

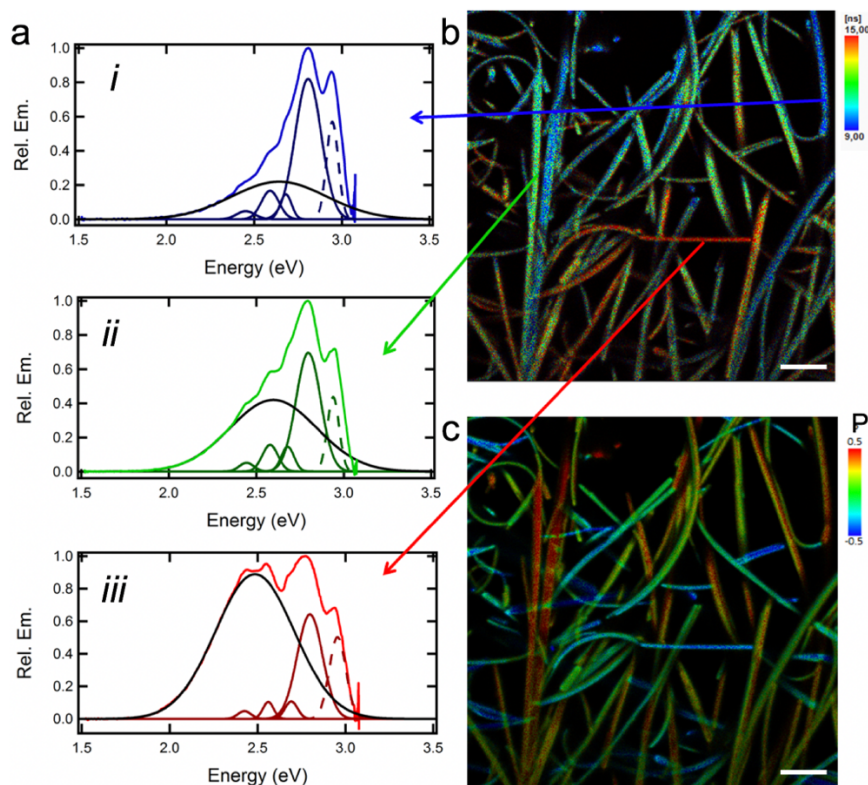


Figure S3. (a) Spectra taken from AF ribbons (0.3 mM DPA16) with very different fluorescence lifetimes: Gaussian deconvolution of emission spectrum of the ribbon with an average lifetime of (i) 9.8 ns, (ii) 11.3 ns and (iii) 16.5 ns. (Black: broad band due to dipolar coupling of defects; dashed Gaussian: adjunct band to complete Gaussian deconvolution since o-o-transition is cut by emission-longpass filter). The vibrational bands are fitted with $\Delta\nu^- = 940 \pm 70 \text{ cm}^{-1}$ but with slightly varying contributions. Ribbons with very different average fluorescence lifetimes show different portions of the red-shifted emission band in their emission spectrum. The emission band of the defects clearly appears in the fits, varying from 471 nm to 478 nm and to 500 nm (from i to iii) indicating different population of defects. A correlation exists between an increasing average fluorescence lifetime and gradually increasing occurrence of a broad defect emission band. (b) Fluorescence lifetime image (average lifetime, FLIM) of the AF ribbons with different lifetimes. (c) Fluorescence polarization image of the same field of view. The different defect emission contribution does not strongly influence the emission polarization.

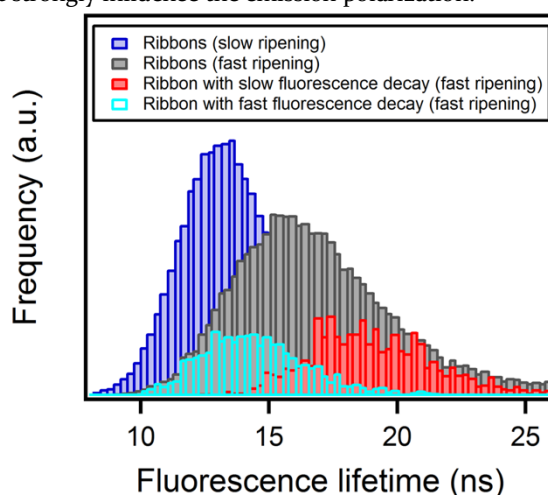


Figure S4. Fluorescence lifetime distributions of AR (slow ripening) and AF (0.3 mM DPA16, fast ripening) ribbons in Figure S3. The fluorescence lifetime in AR ribbons (blue) is shorter ($13.1 \pm 2.6 \text{ ns}$) than the average fluorescence lifetime distribution in AF ribbons (grey) which is broadened and shifted towards $16.1 \pm 4.0 \text{ ns}$. A subset of AF ribbons show longer lifetimes (red) and another subset of AF ribbons shows shorter lifetimes (cyan) similar to the AR ribbons.

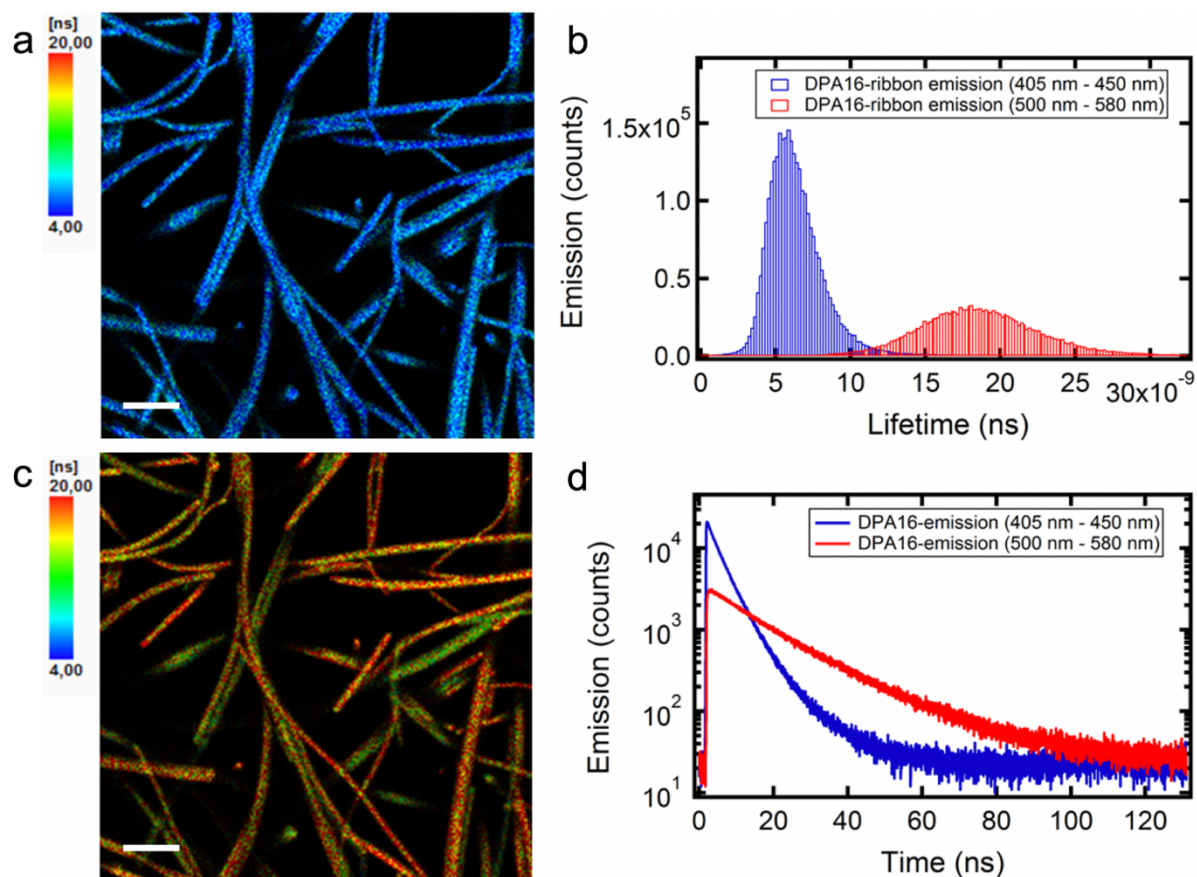


Figure S5. DPA16 AF ribbons (0.3 mM DPA16): (a) FLIM-image (average lifetime) of emission collected after a 'blue' filter (405 nm – 450 nm). Scale bar: 5 μm (b) Average lifetime histogram of emission after a 'blue' (blue histogram) and a 'green' filter (500 nm – 580 nm, red histogram), respectively. (c) FLIM-image (average lifetime) of emission after a 'green' filter. Scale bar: 5 μm (d) Fluorescence decay after a 'blue' (blue curve) and a 'green' (red curve) emission filter. Fitting the fluorescence decays for both the 'blue' emission and for the 'green' emission require at least two exponentials indicating that in each case several fluorescent states are involved.

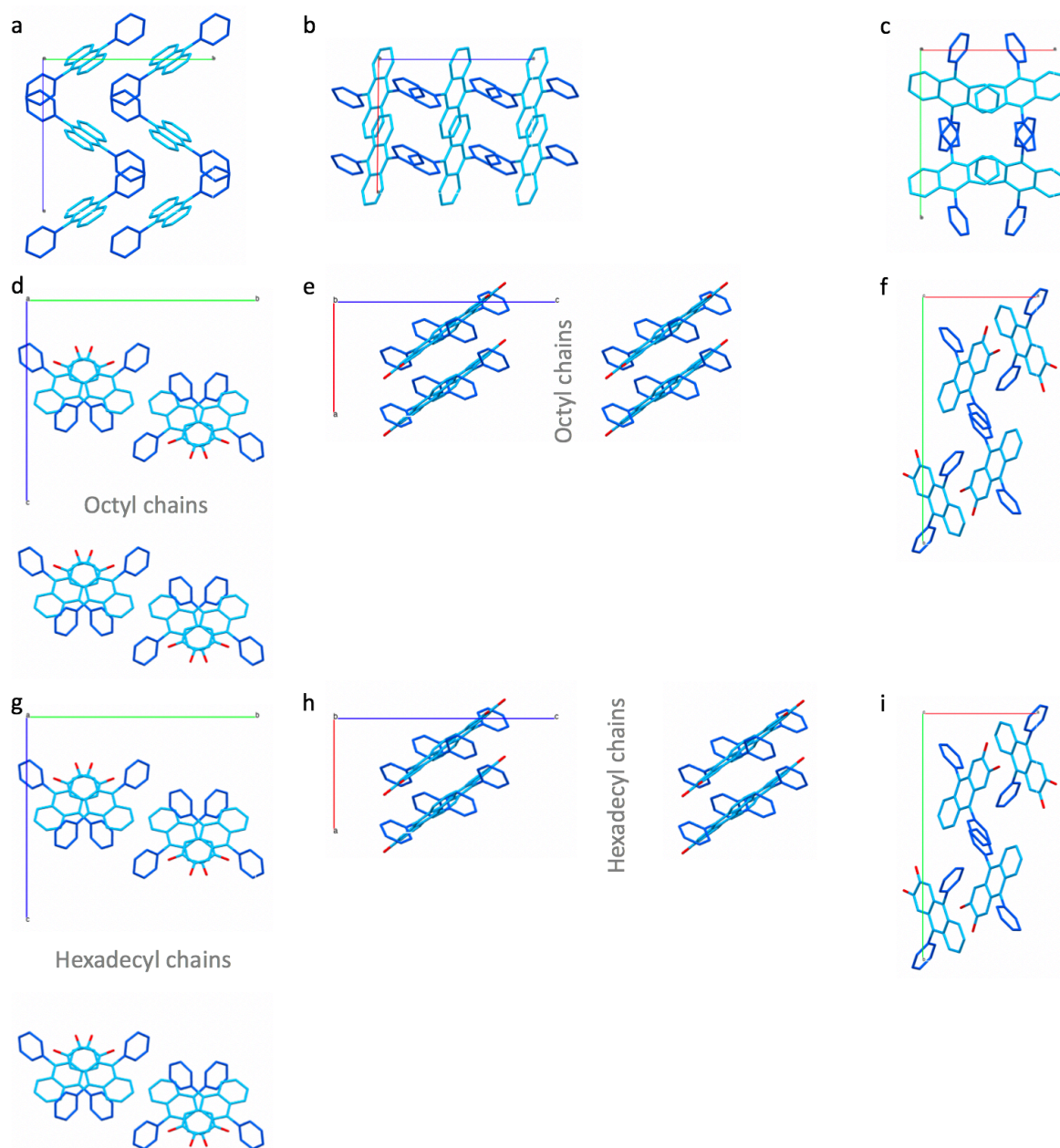


Figure S6. Crystal structures of (a-c) DPA (9,10-diphenylanthracene) and (d-f) DPA8 (2,3-dioctyloxy-9,10-diphenylanthracene), viewed along the three axis (a,d) b/c plane, (b,e) a/c plane, (c,f) a/b plane. The chains in DP8 are omitted for clarity, but their location is indicated in (d,e). The structure of DPA8 differ from the herring-bone structure of crystals of the unmodified DPA.⁶ The distance along the c-axis between the aromatic cores in DPA8 are much larger than in DPA, as the large octyloxychains pack in a layer separating the aromatic cores. (g-i) The same structure is proposed for DPA16 as for DPA8, but with an increased widths of the hexadecyloxychains layer and thus length of the c-axis.

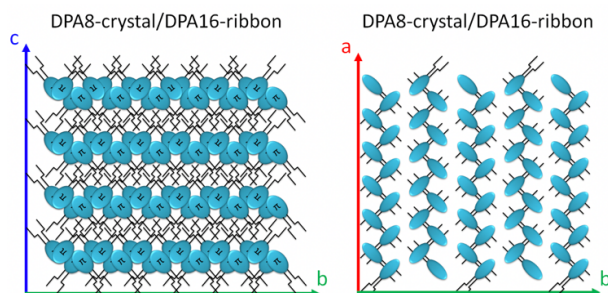


Figure S7. Proposed molecular packing for DPA16 as in Scheme 2, additional views of the b/c plane and the a/b plane.

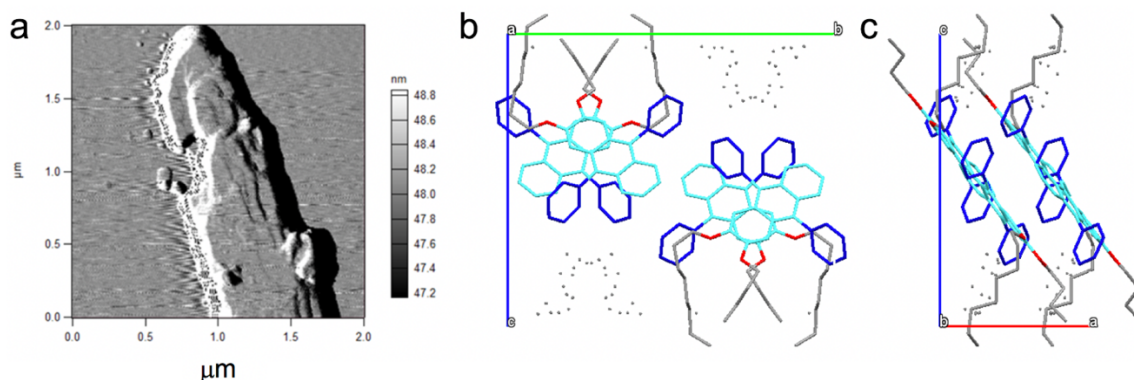


Figure S8. **a)** AFM-amplitude image of an intermittent-mode scan of a small anisotropic DPA8-crystal, showing a succession of flat surfaces with repetitive steps in z-direction (larger crystals could not be imaged by AFM). The AFM-data reveal a layer height of 2.1 ± 0.3 nm, in agreement with the crystal structure of DPA8. The measured height of the layers in DPA8-crystals could correspond to the unit cell length of $b = 2.05$ nm or $c = 1.83$ nm. **b)** X-ray crystal structure of DPA8 viewed along the a-axis (y-direction). **c)** X-ray crystal structure of DPA8 along b-axis (x-direction); the unit cell of DPA8 is monoclinic and of space group $P2_1/a$ with cell lengths of $a = 9.42$ Å, $b = 20.50$ Å and $c = 18.25$ Å. The loose grey dots represent disordered carbon atoms of the octyloxychains that cannot be localized definitely but can be attributed to numerous position-coordinates. This suggests an increased disorder with long alkoxychains. Since the DPA8-crystals served for the elucidation of the crystal structure are gained in a very slow crystallization process (larger crystals), the densest packing possible is expected and the unit cell lengths are minimum values. Since AFM-morphology measurements also reveal some steps smaller than 2.05 nm, it is most probable that the heights measured correspond to the c-axis of the unit cell (1.83 nm in the unit cell). This corresponds to crystals attached on the glass substrate with the a/b-plane (x/y-plane) parallel to the surface (Figure (b)). The correspondence of the measured steps with a height of twice the cell length $a = 0.94$ nm could be possible arithmetically, but seems unlikely.

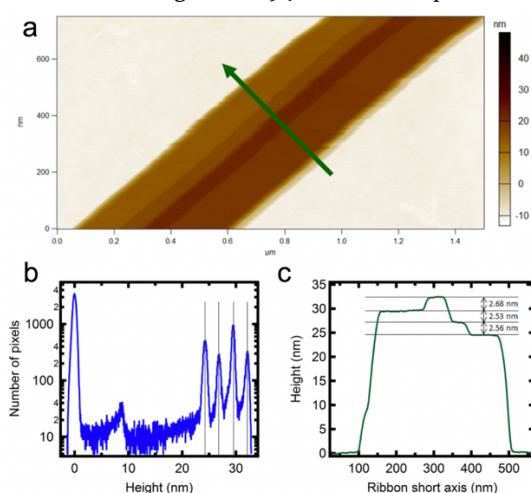


Figure S9. **a)** Topography of an AR ribbon dried on a glass surface (AFM alternating contact mode height retrace); the green arrow indicates the position of the height profile shown in (c). **b)** Histogram of all pixels from the AFM-image with thin height distributions indicating very flat layers. The histogram of pixel values of the full AFM-image show nearly Gaussian profiles at 32.12 ± 0.36 nm, 29.49 ± 0.33 nm, 26.84 ± 0.39 nm and 24.29 ± 0.42 nm which results in 2.6 ± 0.2 nm of mean layer height. **c)** Height profile of the ribbon (green arrow in (a)). The measured step heights are 2.56, 2.53 and 2.68 nm with an estimated error of 0.08 nm. This layered structure of the ribbons suggests a unit cell equivalent to that of DPA8, but with an elongated c-axis of 2.8 ± 0.3 nm. Statistics on a large number of individual ribbons (tens of ribbons from several samples) show that the variations of ± 0.3 nm originate from step heights and are not due to a lack of precision of the measurement. The cause of these height variations could be related to a variable packing density and/or interdigitating of the alkoxy-chains, as supported by X-ray data of DPA8 showing some disorder in the alkoxychain positions.

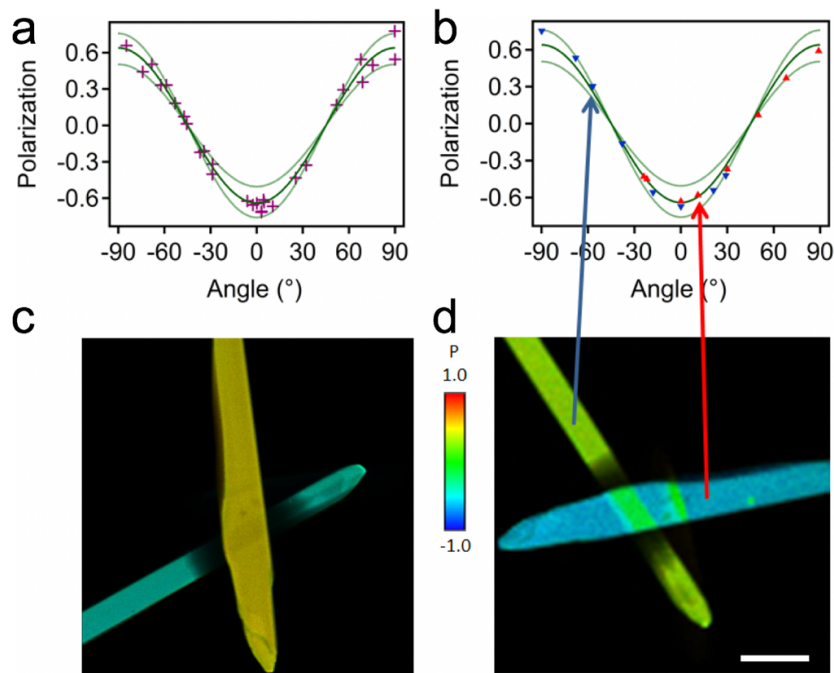


Figure S10. **a)** Polarization plot with data acquired from analyzing several DPA8-crystals. The simulated green curves correspond to the polar plot simulation with crystals oriented with the a/b-plane parallel to the glass. The simulation considers total depolarization of the excitation light due to efficient exciton transfer and hence equal distribution of the absorbed intensity among all the emission dipoles (no photoselection). In addition, a depolarization in emission of 5 % is added in order to take into account the effects due to the use of a high numerical aperture objective.⁷ These polarization simulations do not take into account possible dipolar coupling. The dark green curve corresponds to the exact orientation, the light green curves correspond to the orientation in case of a 10° tilt of the coverslip or the ribbon respectively. These curves indicate the frame in which data points are expected. The small deviations of some polarization values from the ideal simulated curve can be due to a slight tilt angle between optical axis and unit cell axis c. The anisotropic crystals sometimes cross each other and are therefore not always planar with the glass-coverslip, thus not perfectly perpendicular to the laser beam. In addition, due to the contact of the oil immersion objective and a slight pressure on the thin coverslip ($170\ \mu\text{m}$ thick) can bend the substrate. **b)** Polarization plot of measurements when the sample holder was rotated on the microscope objective to vary the angle, only depicting the polarization of the two crystals below, data from one crystal in red and from the other one in blue, indicating that the coverslip was slightly tilted. The model allows fitting the experimental data very well, validating the simulation model based on the crystal structure, the proposed orientation of the crystal unit cell within the object and the depolarization effects. **c)** and **d)** Polarization images of the two DPA8-crystals, the coverslip rotated in between the two acquisitions. Scale bar: $5\ \mu\text{m}$. False color code: Polarization P.

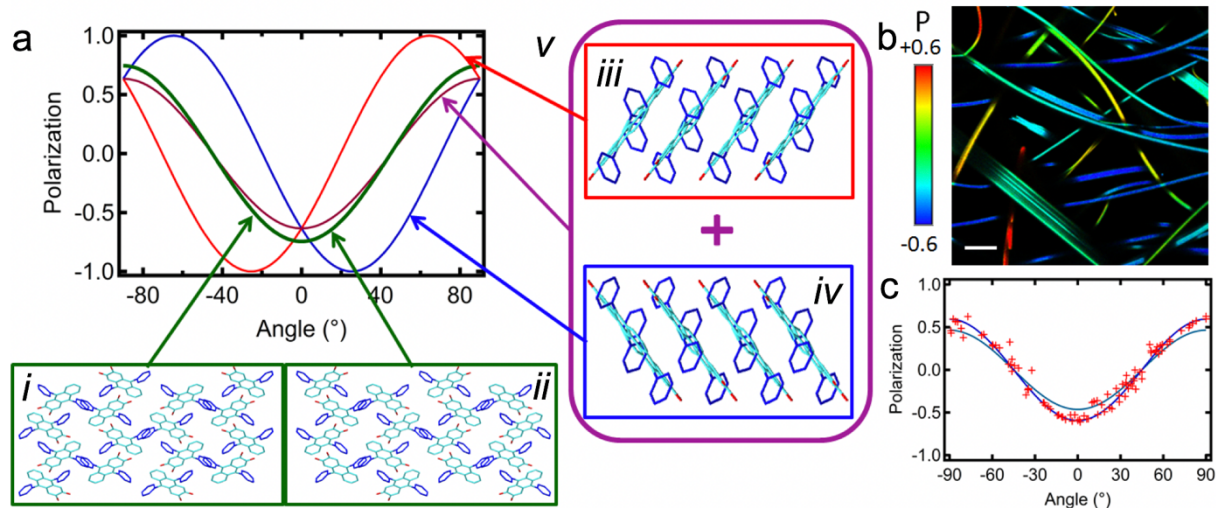


Figure S11: **a)** Simulation of the polarization curve with the a/b-plane exposed to the field of view (green), including the mirror plane which results in the exact same curve (**i** & **ii**); the simulation of the polarization curves for the two opposite sides of the a/c-plane (**iii**: red; **iv**: blue) which are phase-shifted cosine-curves, and a 50/50-mix (**v**: violet) of the two which renders the polarization symmetric around 0° (violet). **b)** Polarization image of slowly ripened AR ribbons at room temperature. **c)** Polarization data extracted from multiple ribbons in **b** and other polarization images, compared to the simulation curves of a 50/50-mix of opposite sides a/c-plane polarization and a simulation relating to the view onto the a/b-plane. These simulations are used based on the premise that the directionality of the layers can be random, and that DPA16-ribbons are thin and flexible to some extent and can twist around their own axis within few tens of micrometers. Therefore the two faces of the ribbons can be exposed towards the optical axis of the microscope resulting in polarization images reflecting the polarization of both faces. Upon strict application of the DPA8-packing, emission from the a/c-plane (edge side 1: **iii**) should display a polarization with a phase-shift relative to the emission from the a/b plane (flat side: **i** & **ii**). Turning the ribbon around its long axis by 180° (edge side 2: **iv**), the opposite phase shift should be observed. However, this is not at all observed. The polarization of a significant part of ribbons, most probably lying on their edge, coincides with a mix of 50 % “edge side 1” and 50 % “edge side 2” (**v**).

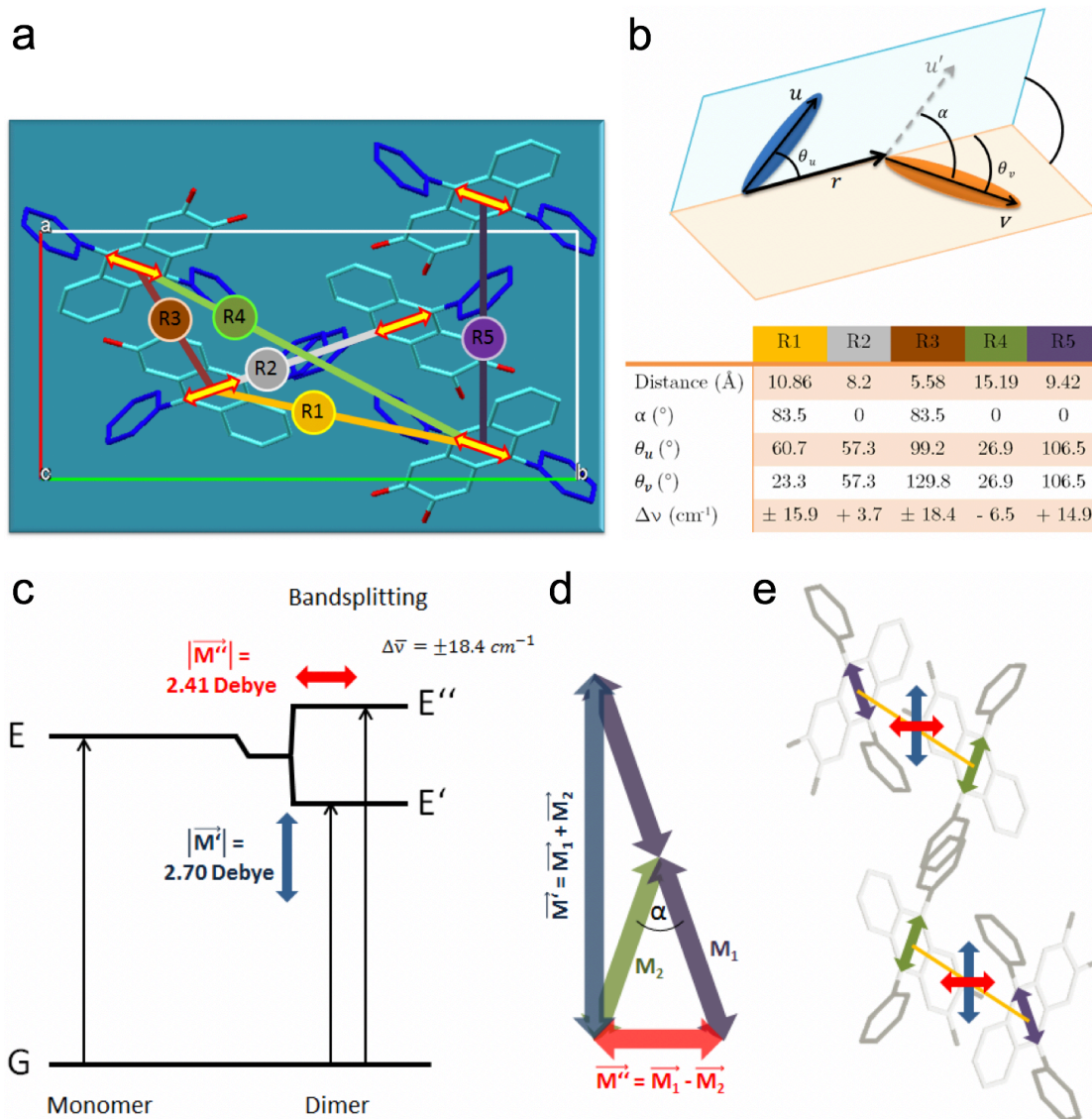


Figure S12. (a) Unit cell of DPA8 with potential dipolar coupling (R1-R5) between different nearest neighbor combinations. In the direction along the a-axis the nearest dipole of the neighboring cell is taken into account additionally. In the other directions the coupling with molecules of neighboring unit cells is negligible. Yellow double arrows indicate the emission dipoles along the transversal axis of the anthracene core. (b) Calculated dipolar coupling (R1-R5) in the DPA8-crystal with inter-dipolar distances, respective angles and resulting energy-splitting $\Delta\nu$. The oscillator strength used for calculations is 0.117. (c-e) Representation of the strongest dipolar coupling (R3) in the DPA8-crystal packing according to Kasha's exciton theory: (c) Energy scheme of ground state G and excited state E for monomer and dimer with energy splitting in the excited state. The "step" in energy between the monomer excited state E and the average of the dimer excited states E'/E'' corresponds to the Van der Waals term mentioned in the main manuscript. (d) Construction of the coupling dipole moments M' and M'' in the a/b-plane. (e) The respective transition dipoles as they are placed and oriented in the unit cell of DPA8 in the a/b-plane. Alkoxychains are omitted for clarity.

Comment to Figure S12: Approximating dipoles by a point, the electronic transition energies are calculated according to the distances and relative orientation estimated from the packing model of DPA8. In DPA16, since the molecular packing proposed is identical, and considering identical or longer distances between dipoles, the coupling energies are expected to be inferior or at most identical. For all closest neighbors, only very weak coupling are obtained due to angles close to 90° or large distances, and a moderate oscillator strength. Therefore allowed transitions are close in energy, resulting in a slight broadening of the absorption bands. Additionally, the ensemble of allowed transitions of emitter couples have the same sum of dipole orientations as the ensemble of the non-coupled monomers, resulting in a non-affected overall emission polarization. These energetically close states can be almost

equi-populated by a combination of thermal population and efficient exciton hopping. Indeed, the spatial proximity of chromophores favors efficient exciton hopping through homo-FRET (Förster Resonance Energy Transfer]: efficiencies within the first shell are estimated to range between 90% and 99.9%, including 99.3% efficiency for the pairs of nearly perpendicular but slip-stacked dipoles R1 & R3. Taking into account these considerations, the emission polarization can be determined by considering the orientations equivalent of non-coupling dipoles in the DPA16 structure described previously, additionally considering a negligible photoselection (hence also the use of equation 2).

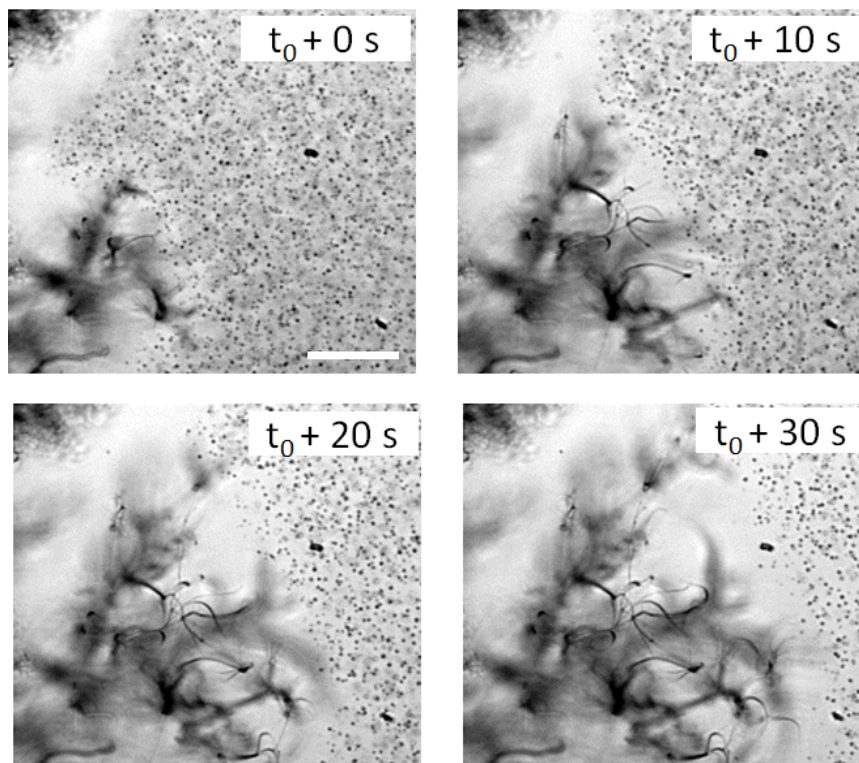


Figure S13. White light transmission microscopy of DPA16 (0.1 mM DPA16) in MeOH/DCM (AF ribbons forming in the microscope). At t_0 (less than half a minute after injection of DPA16/DCM into MeOH); black spots are due to light absorption or scattering by aggregates which have dimension larger than a few hundreds of nm; at $t_0 + 10$ s; at $t_0 + 20$ s; at $t_0 + 30$ s. Scale bar: 10 μm . A high transmission, for example observed between the growing ribbons and finite aggregates, could be due to the low absorption/scattering by dissolved molecules or very small aggregates.

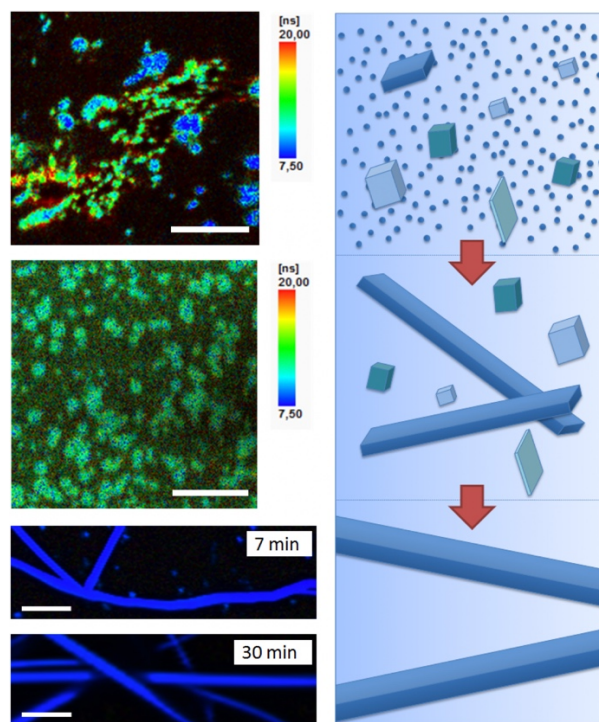


Figure S14. DPA16 (0.1 mM DPA16) in DCM/MeOH (AF ribbons forming in a vial and transferred to the microscope for imaging). **(left, from top to bottom)** FLIM-images of aggregates (average lifetime, scale bar 5 μm) after 2 and 4 minutes, hyperspectral RGB-color converted images of ribbons (scale bar 10 μm) after 7 and 30 minutes. **(right, from top to bottom)** Schematic evolution of the aggregation process from heterogeneous sized aggregates, to aggregates mixed with the first ribbons and finally ribbons (same time-scale left and right).

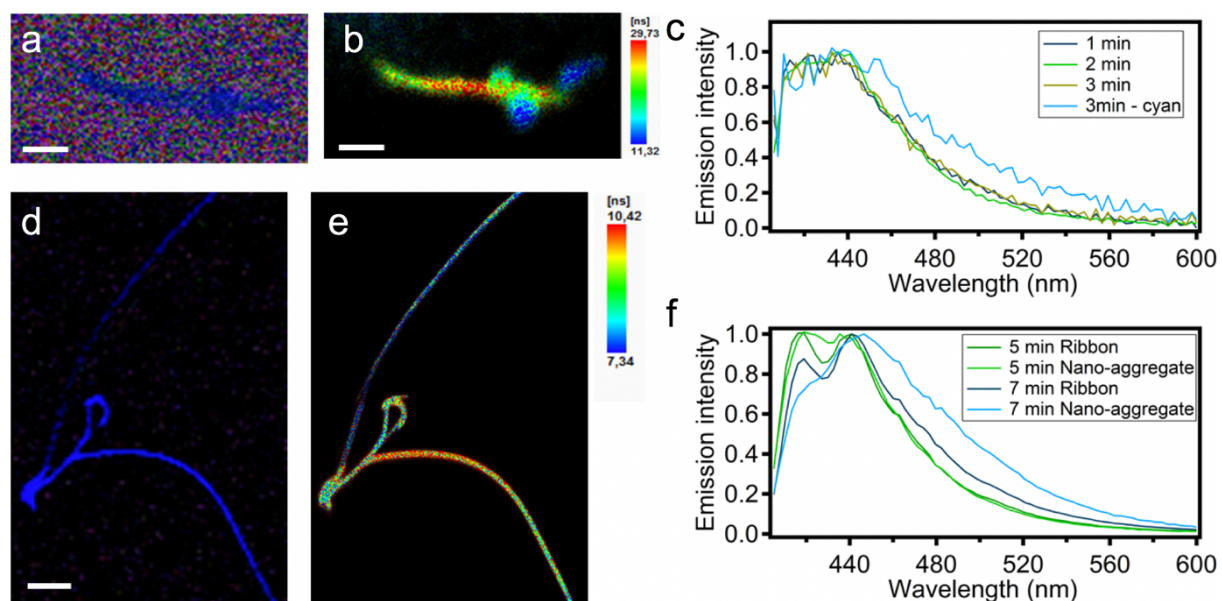


Figure S15. DPA16 (0.1 mM DPA16) in DCM/MeOH (same as Fig. S14). **(a,b,c)** The first anisotropic object after 3 minutes with very heterogeneous average lifetimes within the object: **(a)** Hyperspectral image, **(b)** FLIM (average lifetime), **(c)** Emission spectra of aggregates within the first 3 minutes, the first aggregates with a visible red shoulder in the emission spectrum appear after 3 minutes. **(d,e,f)** The first ribbons appear after 4 minutes and are strongly heterogeneous. The ribbons have grown extremely fast in less than one minute, since only one anisotropic object of 8 μm length was observed after 3 minutes. The areas of ribbons with a short lifetime also emit weaker: **(d)** Hyperspectral image, **(e)** FLIM (Average lifetime), **(f)** Fluorescence spectra of the first ribbons and aggregates at 5 and 7 min. Aggregates which are still visible at a later stage (7 mins) have a stronger red-tail in the spectrum.

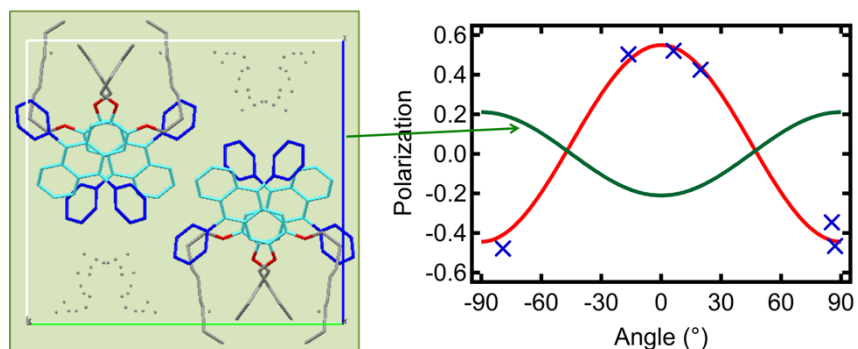


Figure S16. Complement to polarization plot in Figure 6. **BR** ribbons laying on the surface are proposed to have the a/c and the b/c planes parallel to the surface, in contrast to **AR** ribbon (a/c and a/b planes). **(left)** Proposed orientation of molecules packed in **BR** ribbons, with the b/c-plane on the surface; **(right)** green curve: resulting polarization plot (simulated); red curve: simulated polarization plot with the a/c-plane on the surface ($\varphi_{\text{phase}} = 0^\circ$). Blue crosses: P values for non-bundled **BR** ribbon sections (see Figure 6).

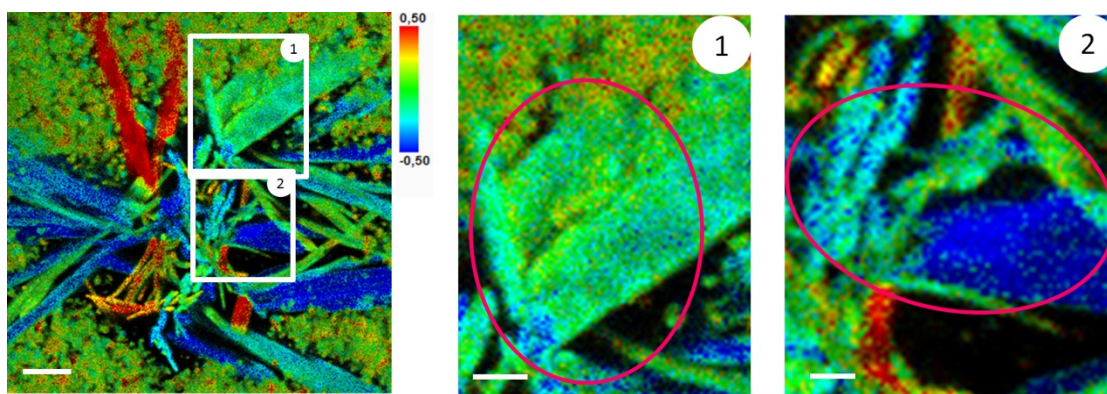


Figure S17. Polarization image (same as Figure 6c) with excerpts (1) and (2) showing additional examples of A-ribbons templated by B-ribbons.

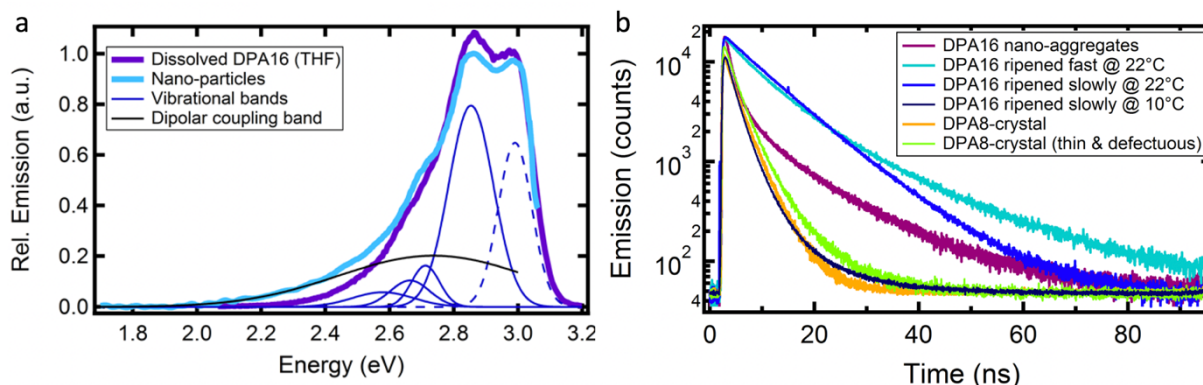


Figure S18. **(a)** Fluorescence spectra of DPA16 dissolved in THF and of DPA16 nano-aggregates, showing coinciding deconvoluted Gaussian-shaped vibrational (blue) bands and defect band (in black). Dashed Gaussian: band representing the o-o-transition that is partially absorbed (and thus deformed) by the emission-longpass filter (405 nm LP). **(b)** Fluorescence decays of DPA16 nano-aggregates (1.4, 10.5 & 15.8 ns), DPA16-ribbons (**AF** ripened fast - 6.1 & 16.3 ns, **AR** ripened slowly at 22°C - 6.9 & 10.8 ns, **BR** ripened slowly at 10°C - 2.0 & 5.4 ns) and two DPA8-crystals (2.0 & 3.8 ns for the 'normal' crystal).

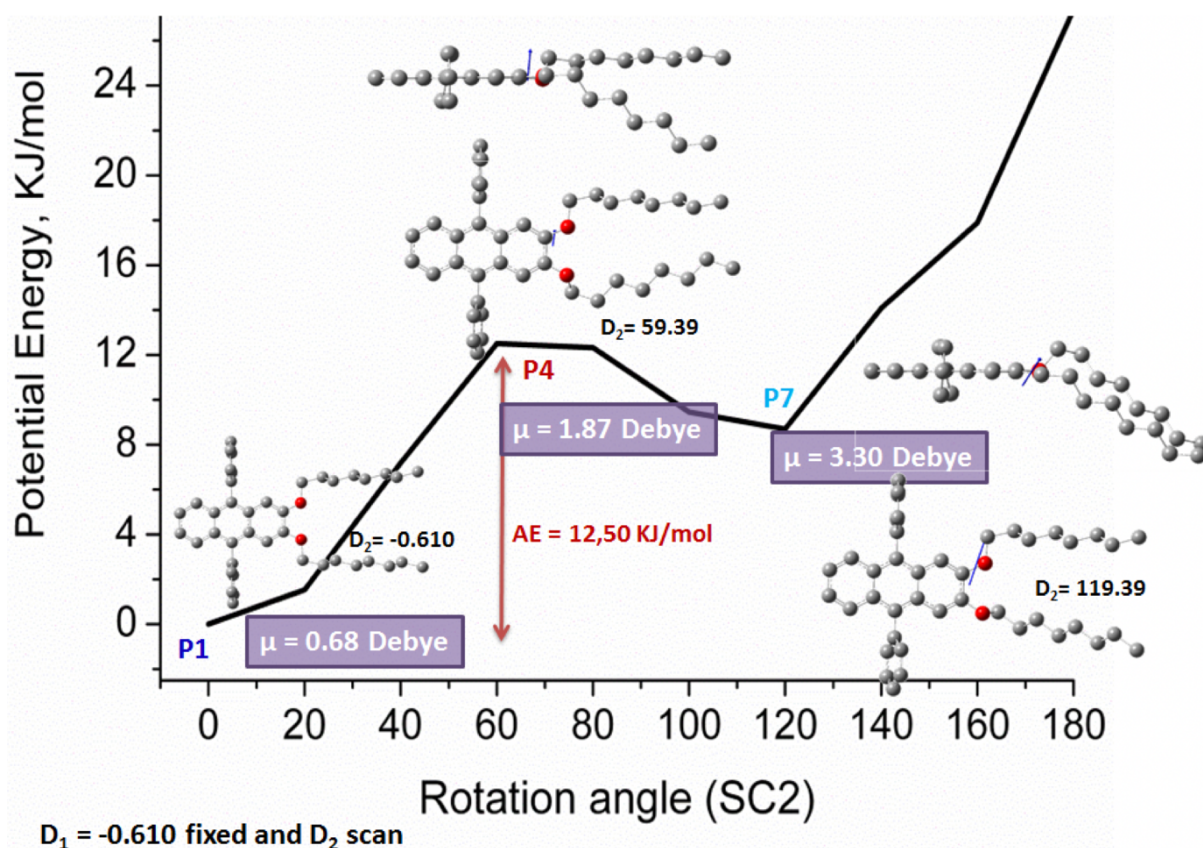
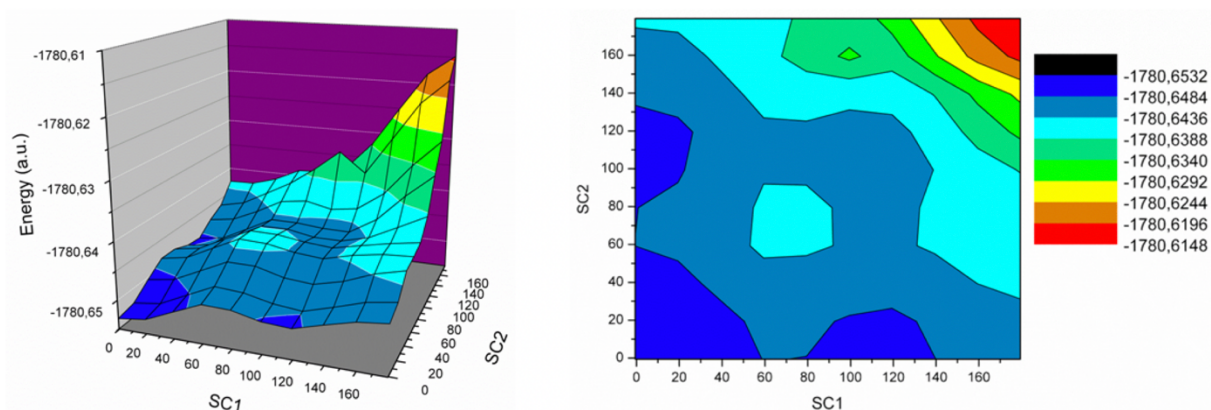


Figure S19. Potential energy surface cross section graph, calculated using Gaussian for DPA8 in methanol. A first global energy minimum (P1) is obtained for the symmetric configuration of the dihedral angles around the two C(Ar)-O bonds showing a dipole moment of 0.68 Debye. To obtain the graph, one of the dihedral angles is varied while keeping the other one constant. A local energy minimum (P7) is observed with an angle of 119.4°, showing a dipole moment of 3.30 Debye. In that state, a phenyl ring distorts out of the perpendicular orientation. To reach P7 starting from P1, an activation barrier of 12.0 kJ/mol has to be overcome and an intermediate conformer reached (P4).



Scan redundant coordinates:

9 steps of 20° = 180°

Dihedral 1 (SC1)

Dihedral 2 (SC2)

Figure S20. Potential energy surfaces calculated using Gaussian for DPA8 in methanol: (left) 3 View, (right) contour potential energy surfaces for rotating both dihedral angles around the two C(Ar)-O bonds in 9 steps of 20°. A global and three local energy minima are obtained.

References

- 1 J. L. Pozzo, G. M. Clavier, M. Colomes and H. Bouas-Laurent, *Tetrahedron*, 1997, **53**, 6377–6390.
- 2 Rigaku, 2013, Version 5.6.2.0 (June 7).
- 3 G. M. Sheldrick, *Acta Cryst.*, 2008, **A64**, 112–122.
- 4 L. J. Farrugia, *J. Appl. Cryst.*, 1999, **32**, 837–838.
- 5 C. F. Macrae, *J. Appl. Cryst.*, 2008, **41**, 466–470.
- 6 T. Salzillo, R. G. Della Valle, E. Venuti, A. Brillante, T. Siegrist, M. Masino, F. Mezzadri and A. Girlando, *J. Phys. Chem. C*, 2016, **120**, 1831–1840.
- 7 K. Bahlmann and S. W. Hell, *Appl. Phys. Lett.*, 2000, **77**, 612.